PERFORMANCE AND ACCURACY OF A MODIFIED FULL MULTIGRID ALGORITHM FOR FLUID FLOW AND HEAT TRANSFER

J. Yan and F. Thiele

Hermann-Föttinger-Institut für Strömungsmechanik, TU Berlin, D-10623 Berlin, Germany

This article aims to assess the performance of a new, full multigrid algorithm in which there is no restriction procedure for variables except for residuals. It simplifies the multigrid strategy and the structure of program. This algorithm is used in combination with the SIMPLE algorithm to solve fluid flows with heat transfer, using collocated grids and higher-order schemes for convective fluxes. Accurate solutions are obtained for lid-driven flow, natural convection in a cavity, and natural convection in an eccentric annulus.

INTRODUCTION

In recent years, significant progress has been made in the development of multigrid methods for the solution of the Navier-Stokes equations. The available results indicate that the multigrid-based solution procedures require less computing time compared to the traditional single-grid methods, which employ algorithms such as SIMPLE. Multigrid methods are efficient not only for laminar isothermal flows [1–4], but also for flows with heat transfer [5–7] as well as for complex turbulent flows [8–10]. In addition, Shyy et al. [11] have extended the algorithm to compressible flows.

So-called full multigrid/full approximation storage (FMG-FAS) methods are widely employed in solving the Navier-Stokes equations. These methods involve the discretization of the equations, the storage of the coefficients, and the solution at every grid level. First the converged solution is obtained on the coarsest grid. This solution is then interpolated to the next finer grid and used there as the starting solution for the multigrid procedure. This procedure continues until the finest grid level is reached, where variables and residuals on the fine grid are restricted to the next coarser one. Initial fluxes through the control-volume faces of the coarse grid are obtained by summing up the corresponding mass fluxes of the fine grid. However, this technique yields mass fluxes that do not match the restricted velocities.

Instead of the FAS algorithm, a new algorithm is proposed in this work, in which only the residuals obtained from the fine grid are restricted to the next coarser one. The variables, used as the starting solutions, are taken directly from the previous cycle on the coarse grid. Thus, there is no restriction procedure for

Received 12 December 1997; accepted 27 April 1998.

Address correspondence to Ph.D. student Jianping Yan, Technische Universität Berlin, Hermann-Föttinger-Institut für Strömungsmechanik, Müller-Breslau Str. 8, D-10623 Berlin, Germany.

Numerical Heat Transfer, Part B, 34:323–338, 1998

1040–7790/98 $12.00 + .00

NOMENCLATURE

D_i	pressure gradient in i direction	θ	dimensionless temperature
Gr	Grashof number	λ	underrelaxation factor
I_H^h	prolongation operator	μ	dynamic viscosity
I_h^H	restriction operator	ν	number of iterations
K_{eq}	equivalent conductivity	ρ	fluid density
L	nonlinear matrix	ϕ	dependent variable
$\dot{m}$	mass flux	∇	gradient operator
Nu	Nusselt number		
p	fluid dynamics pressure	**Subscripts**	
P	dimensionless pressure		
Q_m	mass imbalance	i	inner surface
Pr	Prandtl number	o	outer surface
R	Residual	nb	neighbors of node P
Ra	Rayleigh number	w, s, e, n	west, south, east, north
Re	Reynolds number		
T	fluid temperature	**Superscripts**	
U, V	dimensionless velocity components in x and y directions, respectively	$\hat{}$	starting solution
		$\tilde{}$	approximated solution
V	fluid velocity vector	h	fine grid
X, Y	dimensionless Cartesian coordinates	H	coarse grid
α	thermal diffusivity	$'$	pressure correction
δ	correction in multigrid algorithm		

the variables but only for the residuals, which avoids problems of nonmatching of mass fluxes, and simplifies the multigrid strategy and the structure of the program. The treatment of the pressure correction equation on the coarse grid is achieved in a way similar to the other variables. In the current FMG algorithm, the converged solutions obtained on the coarsest grid are transferred to the second grid level. These converged solutions on the coarsest grid are then taken as the starting solutions for the first multigrid cycle.

The schemes used for the discretization of the convective terms in the momentum and scalar transport equations have a strong influence on the accuracy, efficiency, and convergence of the whole solution procedure. It has been shown (e.g., [10, 12]) that, in order to have the same accuracy, a higher-order scheme requires many fewer grid points than a first-order scheme such as the HYBRID, the UPWIND, or the POWER-LAW differencing scheme [13]. A high-resolution scheme used in combination with any multigrid method can significantly reduce the computational cost, especially for a grid-independent solution.

In this article, a detailed description of the modified V-cycle FMG is presented. The algorithm is applied to accelerate the convergence of a two-dimensional flow solution with heat transfer, employing the higher-order schemes.

MATHEMATICAL FORMULATION

The steady, incompressible fluid flow and heat transfer can be described by conservation equations for mass, momentum, and energy. Neglecting the viscous

dissipation in the energy equation, the system of conservation equations is written as follows:

$$\nabla \cdot (\rho \mathbf{V}) = 0 \tag{1}$$

$$\nabla \cdot (\rho \mathbf{V}\mathbf{V}) = -\nabla p + \nabla \cdot (\mu \nabla \mathbf{V}) + \mathbf{G} \tag{2}$$

$$\nabla \cdot (\rho \mathbf{V} T) = \nabla \cdot (\alpha \nabla T) \tag{3}$$

Due to the Boussinesq approximation, the buoyancy force $\mathbf{G}$ that appears in the momentum Eq. (2) reads

$$\mathbf{G} = \rho_0 \mathbf{g}\, \beta (T - T_0) \tag{4}$$

where β and $\mathbf{g}$ represent the volumetric expansion and gravity acceleration vector, respectively. T_0 denotes the reference temperature and ρ_0 its corresponding density.

DISCRETIZATION METHOD

The conservation equations for all dependent variables can be expressed in the following general form:

$$\nabla \cdot (\rho \mathbf{V} \phi) = \nabla \cdot (\Gamma_\phi \nabla \phi) + S_\phi \tag{5}$$

where ϕ stands for either $\mathbf{V}$ or T. Γ_ϕ represents the exchange coefficient and S_ϕ the source term.

The conservation equation is discretized using the finite-volume technique. A complete review of the discretization procedure is available in [14]; only a brief overview will be given here.

Integrating Eq. (5) over a finite volume and applying the Gauss divergence theorem yields

$$\sum_{\text{all faces}} \mathbf{F} \cdot \mathbf{A} = \sum_{\text{all faces}} (\Gamma_\phi \nabla \phi \cdot \mathbf{A}) + S_\phi \tag{6}$$

Here $\mathbf{F} = \rho \mathbf{V} \phi$ is the convective flux, $\mathbf{A}$ is the cell face area, and S_ϕ is the volume-integrated net source. The discretization of Eq. (6) at a cell P leads to the form

$$-a_P \phi_P + \sum_{\text{nb}} a_{\text{nb}} \phi_{\text{nb}} + S_\phi = 0 \tag{7}$$

where the subscript nb denotes the neighboring nodes of P involved in the polynomials. The coefficient a_{nb} represents the combined convective and diffusive fluxes associated with one of the cell faces, such as

$$a_{\text{nb}} = f(F_{\text{nb}}, D_{\text{nb}}) \tag{8}$$

where F_{nb} and D_{nb} are the convective mass flux and diffusive flux coefficients, respectively. The particular form of the function f depends on the type of the convection scheme used. In this study, the higher-order schemes QUICK [15] and TVD-type MUSCL [16] are used to approximate the convective fluxes, while the diffusive fluxes are discretized via a central differencing scheme.

SOLUTION PROCEDURE

The pressure–velocity coupling is achieved by using the SIMPLE algorithm [13]. The details of the SIMPLE algorithm are independent of the differencing schemes used for the momentum equations. Since a nonorthogonal, nonstaggered grid arrangement is used, the momentum interpolation proposed by Rhie and Chow [17] is employed for calculating the cell-face mass fluxes to avoid pressure oscillations. Equation (7) results in an algebraic system that is solved by the strongly implicit procedure (SIP) of Stone [18].

The solution methods become less efficient on more refined grids because of the iterative coupling of equations and the treatment of the nonlinearities. An efficient solver for inner iterations does not overcome this problem, even if the linearized system of equations is solved directly for each individual equation. The number of outer iterations required to satisfy all equations simultaneously grows almost linearly with increasing number of control volumes.

In this study, the mass, momentum, and energy equations are solved using a coupled multigrid method. The performance of the multigrid method is compared with that of the single-grid method based on the SIMPLE algorithm. In the next subsection, a multigrid algorithm is discussed.

Modified Full Multigrid Algorithm with V-Cycle

The modified full multigrid method adopted here was described in detail by Yan et al. [19]. The strategy is shown in Figure 1, where the arrow ↘ symbolizes the transfer of residuals from the fine grid to the next coarser one. The symbol ↗ holds for the processes from the coarse grid to the next finer one. They include the calculation of the coarse grid corrections, the prolongation of these corrections or

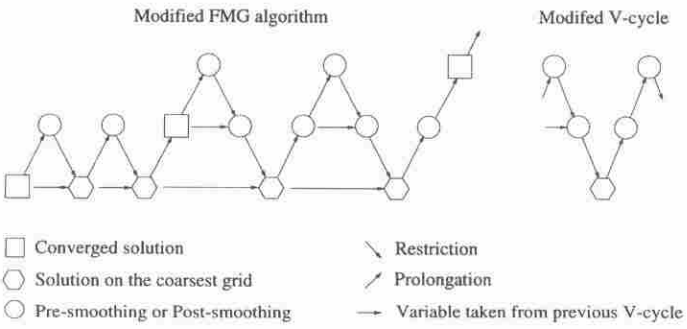

Figure 1. Modified FMG algorithm and V-cycle.

the converged solutions, and the correction of the previous intermediate solutions on the fine grid. The arrow $\rightarrow$ symbolizes the processes in which the variables are taken from the previous V-cycle.

Multigrid Method with SIMPLE Algorithm on the Coarse Grid

Applying the method proposed, Eq. (7) for momentum can be rewritten as follows:

$$L\{u_i\} + D_i(p) + S\{u_i\} = f\{u_i\} \tag{9}$$

where $L\{u_i\}$ represents the quantity $-a_P\phi_P + \Sigma a_{\text{nb}}\phi_{\text{nb}}$, and $D_i(p)$ and $S\{u_i\}$ denote the pressure gradient term in the i direction and the source term, respectively. $f\{u_i\}$ is the right-hand-side term; it is zero on the finest grid and nonzero on any coarse grid.

After performing ν_1 outer iteration sweeps with the SIMPLE algorithm on the fine grid denoted by superscript h, the intermediate solutions of velocity components and pressure are obtained. In general, the momentum equations are not converged and have the residuals R^h, which can be expressed as

$$\bar{L}^h\{\bar{u}_i^h\} + \bar{D}_i^h(\bar{p}^h) + \bar{S}^h\{\bar{u}_i^h\} = f^h\{u_i\} + \bar{R}^h\{\bar{u}_i^h\} \tag{10}$$

where $\bar{u}_i^h$ and $\bar{p}^h$ denote the intermediate solutions of the velocity components and pressure, respectively, and $R^h\{\bar{u}_i^h\}$ is the residual of the u_i equation.

In order to obtain the converged solutions, the following corrections for velocity components and pressure are introduced:

$$\tilde{u}_i^h = \bar{u}_i^h + \delta u_i^h \qquad \tilde{p}^h = \bar{p}^h + \delta p^h \tag{11}$$

which make the residuals vanish:

$$\tilde{L}^h\{\tilde{u}_i^h\} + \tilde{D}_i^h(\tilde{p}^h) + \tilde{S}^h\{\tilde{u}_i^h\} = f^h\{u_i\} \tag{12}$$

Subtracting Eq. (10) from Eq. (12) yields

$$\tilde{L}^h\{\tilde{u}_i^h\} + \tilde{D}_i^h(\tilde{p}^h) + \tilde{S}^h\{\tilde{u}_i^h\} = \underbrace{\bar{L}^h\{\bar{u}_i^h\} + \bar{S}^h\{\bar{u}_i^h\} + \bar{D}_i^h\{\bar{p}^h\} - \bar{R}^h\{\bar{u}_i^h\}}_{\text{constant}} \tag{13}$$

This equation is used as the basis for multigrid coupling. A similar equation for T reads

$$\tilde{L}^h\{\tilde{T}^h\} + \tilde{S}^h\{\tilde{T}^h\} = \underbrace{\bar{L}^h\{\bar{T}^h\} + \bar{S}^h\{\bar{T}^h\} - \bar{R}^h\{\bar{T}^h\}}_{\text{constant}} \tag{14}$$

Applying the multigrid method, the corrections can be obtained on the coarse grid. As in the CS method, only the residuals are restricted to the coarse grid and the multigrid algorithm described above is applied because of the nonlinearity of velocities and other variables. The momentum equation on the coarse grid denoted by superscript H now reads

$$\tilde{L}^H\{\tilde{u}_i^H\} + \tilde{D}_i^H(\tilde{p}^H) + \tilde{S}^H\{\tilde{u}_i^H\}$$

$$= f^H\{u_i\} = \underbrace{\hat{L}^H\{\hat{u}_i^H\} + \hat{D}_i^H\{\hat{p}^H\} + \hat{S}^H\{\hat{u}_i^H\} - \left[I_h^H\right]\bar{R}^h\{\bar{u}_i^h\}}_{\text{constant}} \tag{15}$$

Here, the variables $\hat{u}_i^H$ and $\hat{p}^H$ are the starting solutions, while $\tilde{u}_i^H$ and $\tilde{p}^H$ denote the approximations on the coarse grid. In the traditional FAS algorithm, the starting solutions except for pressure are restricted from the fine grid. In the current algorithm, $\hat{u}_i^H$ and $\hat{p}^H$ are taken from the previous cycle. On the right-hand side, the term $[I_h^H]\bar{R}^h\{\bar{u}_i^h\}$ is the restricted residual obtained from the fine grid, whereas the other terms are calculated on the coarse grid using the starting solutions. The right-hand-side terms remain unchanged within the iterative process on the coarse grid.

The equation for T on the coarse grid results in

$$\tilde{L}^H\{\tilde{T}^H\} + \tilde{S}^H\{\tilde{T}^H\} = f^H\{T\} = \underbrace{\hat{L}^H\{\hat{T}^H\} + \hat{S}^H\{\hat{T}^H\} - \left[I_h^H\right]\bar{R}^h\{\bar{T}^h\}}_{\text{constant}} \tag{16}$$

where the variable $\hat{T}^H$ is taken from the previous cycle and used as an initial guess, and $\tilde{T}^H$ denotes the approximation on the coarse grid. On the right-hand side, the term $[I_h^H]\bar{R}^h\{\bar{T}^h\}$ is the restricted residual obtained from the fine grid, whereas the other terms are calculated on the coarse grid based on the starting solutions.

The treatment of the pressure correction equation in the multigrid algorithm deserves more attention. The pressure correction equation can be written in the general form

$$Q_m = L\{p'\} + Q_m^* = f\{p'\} \tag{17}$$

where $Q_m^* = \dot{m}_e^* + \dot{m}_w^* + \dot{m}_n^* + \dot{m}_s^*$ and $Q_m = \dot{m}_e + \dot{m}_w + \dot{m}_n + \dot{m}_s$ in cases of 2D. The terms $\dot{m}^*$ and $\dot{m}$ denote the mass fluxes before and after the correction with the pressure correction p', respectively; Q_m^* and Q_m are the corresponding mass imbalances. The term $f\{p'\}$ on the right-hand side is zero on the finest grid and nonzero on any coarse grid.

After some SIMPLE iterations on the fine grid, the solution of equations is not converged and Eq. (17) still has the residual $R^h\{p'\}$:

$$R^h\{p'\} = Q_m^h - f^h\{p'\} \tag{18}$$

The pressure correction equation on the coarse grid can be expressed as

$$Q_m^H = L\{p'^H\} + Q_m^{*H} = f^H\{p'\} = \underbrace{\hat{Q}_m^H - \left[I_h^H\right] R^h\{p'\}}_{\text{constant}} \tag{19}$$

where the $\hat{Q}_m^H$ is the starting mass imbalance taken from the previous cycle. The right-hand-side term $f^H\{p'\}$ remains constant during the iterations on the coarse grid.

As Eq. (19) is solved with a nonzero right-hand-side term $f^H\{p'\}$ on the coarse grid, the global mass flux should be corrected with the sum of $f^H\{p'\}$ through the entire domain $\Sigma f^H\{p'\}$. In cases of open through-flow geometries, we assume that the sum of mass fluxes at the inlet boundary is equal to the sum of mass fluxes at the outlet one on the finest grid. On the coarse grid, $\Sigma f^H\{p'\}$ should be added to the sum of inlet mass fluxes to satisfy the global conservation condition.

Beginning with the starting quantities $\hat{u}_i^H$, $\hat{p}^H$, and $\hat{T}^H$, ν_1 SIMPLE iterations are performed to obtain the approximate solutions on the coarse grid. The coarse-grid corrections are then calculated as

$$\delta u_i^H = \tilde{u}_i^H - \hat{u}_i^H \qquad \delta p^H = \tilde{p}^H - \hat{p}^H \qquad \delta T^H = \tilde{T}^H - \hat{T}^H \tag{20}$$

Once these coarse-grid corrections are obtained, they are prolongated to the fine grid and added to the previous intermediate solutions:

$$\bar{\bar{u}}_i^h = \bar{u}_i^h + \lambda_u\left[I_H^h\right] \delta u_i^H \qquad \bar{\bar{p}}^h = \bar{p}^h + \lambda_p\left[I_H^h\right] \delta p^H \qquad \bar{\bar{T}}^h = \bar{T}^h + \lambda_T\left[I_H^h\right] \delta T^H \tag{21}$$

Here, a stability measure is introduced into Eq. (21) by underrelaxing the corrections with λ ($0 < \lambda \leqslant 1$) to compensate for a lack of smoothness in the coarse-grid corrections.

It should be noted that the pressure correction S_p^H is calculated directly by Eq. (20). This is different from other works, in which the so-called correction of pressure correction is calculated. In Eq. (19), the right-hand-side term consists of two parts: the first part is taken from the previous cycle, while the other is restricted from the fine grid. The treatment is the same for all variables.

Moreover, the corrections to the mass fluxes on the fine grid are calculated by using velocity corrections. They are added to the previous mass fluxes. In addition, postsmoothing with ν_2 SIMPLE iterations is performed.

Restriction and Prolongation

In this work, only residuals are restricted from the fine grid to the next coarser one. The summation of the corresponding fine-grid residuals provides a consistent restriction method. This method is applied to all equations. The converged solutions and the coarse-grid corrections are transferred to the fine grid using a standard bilinear interpolation in 2D and trilinear interpolation in 3D.

Boundary Conditions

On all grid levels, the boundary conditions are treated in the same way as in any single-grid algorithm. Neumann conditions used for pressure correction at boundaries on the finest grid are also applied to the pressure correction on any coarse grid.

RESULTS

The modified full multigrid method described in the previous section is implemented to solve fluid flow and heat transfer. Here, we focus on two-dimensional test cases. Solutions are considered to be convergent if the summation of the absolute residuals over all cells is less than 10^{-4}. To enhance stability and smoothness, underrelaxation is employed, with related factors being 0.7 for velocities, 0.3 for pressure correction, and 0.8 for temperature. All calculations are performed with FMG with fixed V-cycle. No attempt has been made to optimize these parameters in favor of the computations.

Lid-Driven Square Cavity Flow

The performance of the proposed multigrid method is demonstrated by the calculation of the lid-driven square cavity flow. For this isothermal problem, the energy equation does not need to be considered, and the buoyancy term **G** can be dropped in Eq. (2). Using the dimensionless quantities $U = u/U_0$, $X = x/L$, etc., the governing equations become

$$\frac{\partial U}{\partial X} + \frac{\partial V}{\partial Y} = 0 \tag{22}$$

$$U\frac{\partial U}{\partial X} + V\frac{\partial U}{\partial Y} = -\frac{\partial P}{\partial X} + \frac{1}{\mathrm{Re}}\left(\frac{\partial^2 U}{\partial X^2} + \frac{\partial^2 U}{\partial Y^2}\right) \tag{23}$$

$$U\frac{\partial V}{\partial X} + V\frac{\partial V}{\partial Y} = -\frac{\partial P}{\partial Y} + \frac{1}{\mathrm{Re}}\left(\frac{\partial^2 V}{\partial X^2} + \frac{\partial^2 V}{\partial Y^2}\right) \tag{24}$$

where Re is the Reynolds number defined as $\mathrm{Re} = LU_0/\nu$.

To investigate the behavior of the multigrid method, calculations are performed for a Reynolds number of $\mathrm{Re} = 10^3$ based on lid velocity $U_0 = 1$ m/s and $L = 1$ m. No-slip wall boundary conditions are used. As seen in Figure 2, a sequence of four grid levels ranging from 16×16 to 128×128 grid cells has been adopted. In general, the numbers of iterations for pre-/postsmoothing are $\nu_1 = 3$ and $\nu_2 = 2$, respectively. The number of iterations for smoothing on the coarsest grid is $\nu_0 = 8$. The QUICK and MUSCL schemes are employed. All computations start with an initial field of zero velocities and zero pressure.

The evaluation of the method is based on the number of work units (WUs) required to obtain a converged solution as well as the corresponding CPU time. WU is a computer-independent measure that is defined as the computational work

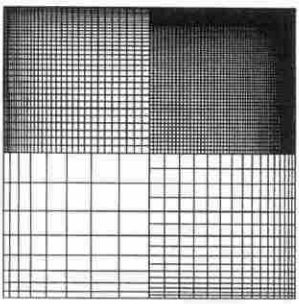

Figure 2. Segments of the four grids (one quarter of each).

required for $\nu_1 + \nu_2$ outer relaxation sweeps on the finest grid. Tables 1 and 2 show that the number of iterations increases almost linearly with the number of control volumes for single-grid computations. In contrast, the multigrid methods even display a decrease. Calculations using the MUSCL scheme rather than the QUICK scheme need somewhat more CPU time to obtain a converged solution. However, the MGM has only a weak effect on the convection schemes.

The convergence behavior of the single-grid and multigrid calculations using the MUSCL and QUICK schemes is displayed in Figure 3. The multigrid method results in a significantly faster convergence of the solution procedure. In Figure 4*a* the primary vortex and the two secondary vortices at the bottom corners of the cavity can be clearly distinguished. Figure 4*b* compares present results for the velocities along the vertical and horizontal cavity midlines. Both convection schemes, MUSCL and QUICK, lead to identical results, which are in very good agreement with the calculation obtained by Ghia et al. [20].

Table 1. Number of WUs and CPU time using MUSCL scheme for lid-driven square cavity flow

	Single-grid MUSCL		Multigrid MUSCL		
Grid	WU	CPU time	WU	CPU time	Speed-up
16 × 16	26	2.53	26	2.53	1.000
32 × 32	46	11.64	15	9.11	1.278
64 × 64	99	92.98	8	20.59	4.516
128 × 128	313	1,253.09	5	49.80	25.162

Table 2. Number of WUs and CPU time using QUICK scheme for lid-driven square cavity flow

	Single-grid QUICK		Multigrid QUICK		
Grid	WU	CPU time	WU	CPU time	Speed-up
16 × 16	30	2.59	30	2.59	1.000
32 × 32	45	10.29	15	8.69	1.184
64 × 64	99	83.19	8	18.90	4.402
128 × 128	315	1,145.27	4	43.18	26.523

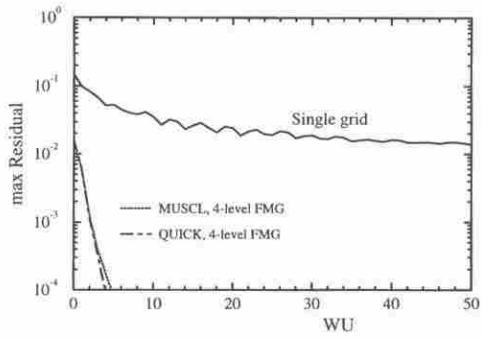

Figure 3. Convergence history for lid-driven cavity flow at Re = 1,000.

Natural-Convection Flow in a Cavity

A common benchmark test for numerical computations is the flow in a square cavity with one hot vertical wall and one cold facing wall. The horizontal walls are assumed to be adiabatic. The same grid structure as before is used for the computation. Here, the governing equations are nondimensionalized, with length, velocity, and temperature scales as L, $(g\beta\Delta TL)^{1/2}$, and $\Delta T = T_h - T_c$, respectively,

$$\frac{\partial U}{\partial X} + \frac{\partial V}{\partial Y} = 0 \tag{25}$$

$$U\frac{\partial U}{\partial X} + V\frac{\partial U}{\partial Y} = -\frac{\partial P}{\partial X} + \frac{1}{\sqrt{\mathrm{Gr}}}\left(\frac{\partial^2 U}{\partial X^2} + \frac{\partial^2 U}{\partial Y^2}\right) \tag{26}$$

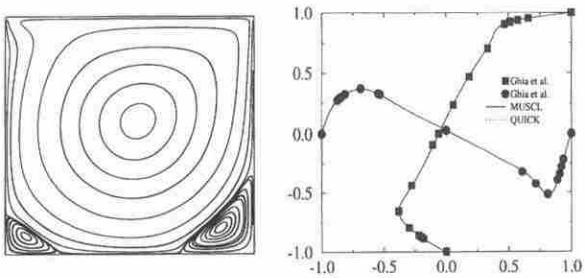

(*a*) (*b*)

Figure 4. Lid-driven cavity flow at Re = 1,000: (*a*) streamlines; (*b*) comparisons of u and v velocity components along the vertical and horizontal midlines.

$$U\frac{\partial V}{\partial X} + V\frac{\partial V}{\partial Y} = -\frac{\partial P}{\partial Y} + \frac{1}{\sqrt{\mathrm{Gr}}}\left(\frac{\partial^2 V}{\partial X^2} + \frac{\partial^2 V}{\partial Y^2}\right) + \theta \tag{27}$$

$$U\frac{\partial \theta}{\partial X} + V\frac{\partial \theta}{\partial Y} = \frac{1}{\mathrm{Pr}\sqrt{\mathrm{Gr}}}\left(\frac{\partial^2 \theta}{\partial X^2} + \frac{\partial^2 \theta}{\partial Y^2}\right) \tag{28}$$

where the Grashof number Gr, the Prandtl number Pr, and the Rayleigh number Ra are defined as follows:

$$\mathrm{Gr} = \frac{g\beta L^3(T_h - T_c)}{\nu^2} \qquad \mathrm{Pr} = \frac{\nu}{\alpha} \qquad \mathrm{Ra} = \mathrm{Gr}\cdot\mathrm{Pr} \tag{29}$$

With no-slip conditions on all walls, the dimensionless temperatures on the cold and hot walls vary between 0 and 1, respectively. Due to the inherent conservation in the finite-volume method used here, the average Nusselt number is evaluated by using the temperature gradient at the wall:

$$\overline{\mathrm{Nu}} = \overline{\mathrm{Nu}}_{\mathrm{wall}} = -\int_0^1 \frac{\partial \theta}{\partial X}\, dY \tag{30}$$

Here, the calculation for $\mathrm{Ra} = 10^6$ and $\mathrm{Pr} = 0.71$ is carried out using the MUSCL scheme. As reported in Table 3, the speed-up decreases significantly in comparison to the lid-driven cavity flow, due to the weak coupling of temperature and velocities. The average Nusselt number seems to converge monotonically toward grid-independent value. Compared with the benchmark solution ($\overline{\mathrm{Nu}} = 8.80$) presented by G. de Vahl Davis [21], the agreement is very good.

Figure 5 shows the convergence histories. The streamlines and isotherms in Figure 6 show the complex structure of the flow with natural convection.

Natural Convection in an Eccentric Annulus

A pronounced test case is the flow between two horizontal eccentric cylinders of radii r_o with $r_o > r_i$, located at o and o' as shown in Figure 7. The eccentricity of the inner cylinder is defined by the distance E. The inner and outer surfaces are maintained at two different temperatures, T_h and T_c, with $T_h > T_c$. As the length scale is the average gap $L = (r_o - r_i)$, the dimensionless governing equations are the same as Eqs. (25)–(28).

Table 3. Number of WUs and CPU time for natural convection in a cavity at $\mathrm{Ra} = 10^6$ and $\mathrm{Pr} = 0.71$

	Single-grid		Multigrid			
Grid	WU	CPU time	WU	CPU time	Speed-up	$\overline{\mathrm{Nu}}$
16 × 16	18	2.41	18	2.41	1.000	9.224
32 × 32	45	15.80	13	9.37	1.668	8.963
64 × 64	130	172.75	29	66.88	2.583	8.857
128 × 128	468	2,748.07	82	757.12	6.589	8.841

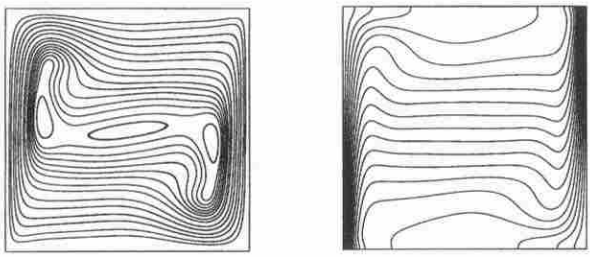

(*a*) (*b*)

Figure 6. Streamlines and isotherms for natural convection in a cavity.

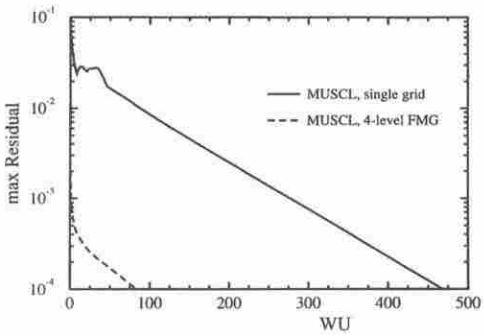

Figure 5. Convergence history for natural convection in a cavity at $Ra = 10^6$ and $Pr = 0.71$.

This natural-convection flow has broad industrial applications involving thermal insulation engineering, such as steam lines, gas lines in gas-cooled nuclear reactors, cryogenics, and storage of thermal energy. Experimental studies of eccentric geometry such as those of Koshmarov and Ivanov [22], Probert et al. [23], Sande and Hamer [24], and Naylor et al. [25], are concerned primarily with the variation of overall heat transfer with eccentricity and Rayleigh number. Detailed

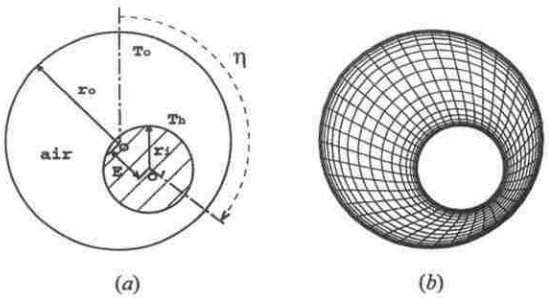

(*a*) (*b*)

Figure 7. (*a*) Geometry. (*b*) Second grid level.

interferometric results for both vertical and nonvertical eccentricities are presented by Kuehn and Goldstein [26] in the boundary-layer regime ($3 \times 10^4 < \mathrm{Ra} < 10^5$), where the overall heat transfer coefficients are all within 10% of the concentric geometry for $E/L = \frac{1}{3}, \frac{2}{3}$. Numerical studies for the concentric and eccentric annulus have been performed over a wide range of eccentricities and Rayleigh numbers.

In this test case, the dimensionless temperatures at the inner and outer surfaces are prescribed by 1 and 0, respectively. The heat transfer data is presented in terms of the equivalent conductivities K_{eq_i} and K_{eq_o} at the inner and outer surfaces, respectively, which represent the influence of the buoyancy-driven fluid motion:

$$K_{\mathrm{eq}_i} = \left| \frac{\partial \theta}{\partial n} \right|_i r_i \ln\left(\frac{r_o}{r_i}\right) \tag{31}$$

$$K_{\mathrm{eq}_o} = \left| \frac{\partial \theta}{\partial n} \right|_o r_o \ln\left(\frac{r_o}{r_i}\right) \tag{32}$$

Here, n is the local coordinate normal to the surfaces. The integration for the local heat fluxes on the cylinder surfaces leads to the average conductivity $\overline{K_{\mathrm{eq}}}$ in the annulus:

$$\overline{K_{\mathrm{eq}_i}} = \frac{\sum K_{\mathrm{eq}_i} \Delta S_i}{\sum \Delta S_i} = \overline{K_{\mathrm{eq}_o}} = \frac{\sum K_{\mathrm{eq}_o} \Delta S_o}{\sum \Delta S_o} = \overline{K_{\mathrm{eq}}} \tag{33}$$

where ΔS_i and ΔS_o denote the discretized arc length of the inner and outer surfaces, respectively.

Calculations of the flow field are performed at $\mathrm{Ra} = 10^3$, $\mathrm{Pr} = 0.71$ and $E/L = 0.6$ using the MUSCL scheme for various azimuthal angles η. Table 4 compares the experimental and numerical results of the averaged conductivity $\overline{K_{\mathrm{eq}}}$, which are in good agreement. The experimental average conductivity (1.339) for the case $\eta = 0°$ is greater than that for the case $\eta = 45°$ (1.335). The numerical results indicate that the value of $\overline{K_{\mathrm{eq}}}$ increases with the angle η, due to the development of larger and stronger convective cells.

Table 4. Comparisons between the experimental and numerical values of average conductivities at $\mathrm{Ra} = 10^3$ and $\mathrm{Pr} = 0.71$

η	$\overline{K_{\mathrm{eq}}}$ (exp.)	$\overline{K_{\mathrm{eq}}}$ (num.)	Percentage difference
0°	1.339	1.340	0.075%
45°	1.335	1.354	1.423%
90°	1.358	1.376	1.325%
135°	1.421	1.443	1.548%
180°	1.448	1.478	2.072%

Table 5. Number of WUs and CPU time for natural convection in an eccentric annulus at $Ra = 10^3$, $Pr = 0.71$, and $\eta = 135°$

	Single-grid		Multigrid			
Grid	WU	CPU time	WU	CPU time	Speed-up	$\overline{K_{eq}}$
20×10	11	1.56	11	1.56	1.000	1.448
40×20	21	8.78	8	5.67	1.548	1.445
80×40	74	136.77	15	36.22	3.776	1.444
160×80	284	2,273.43	40	364.01	6.245	1.443

Table 5 shows the number of WUs, CPU time, speed-up factor, and average conductivity $\overline{K_{eq}}$ for the case $\eta = 135°$, which differs slightly on various grid levels. The convergence histories are shown in terms of WU in Figure 8. The main features of the flow are shown in Figure 9 by the distributions of streamlines and isothermal lines for $\eta = 135°$. The distribution of the isothermal lines shows that the heat conduction is predominant in the narrowest part of the gap. A high temperature gradient due to the rising plume near the top of the outer surface results in two maximum values for the local K_{eq} distribution at the outer surface.

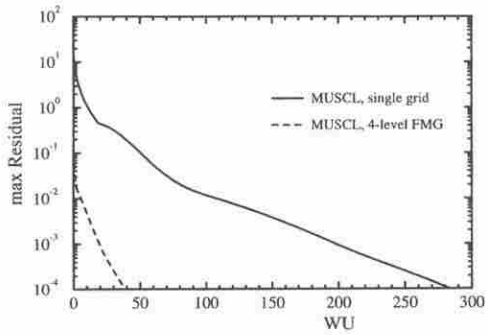

Figure 8. Convergence history for natural convection in an eccentric annulus at $Ra = 10^3$ and $Pr = 0.71$.

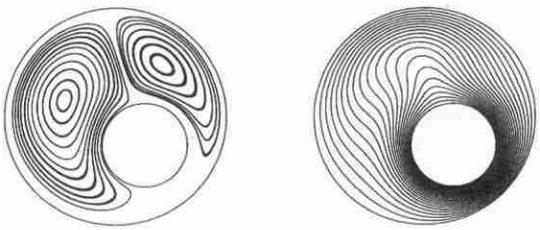

(*a*) (*b*)

Figure 9. Streamlines and isotherms for natural convection in an eccentric annulus at $Ra = 10^3$, $Pr = 0.71$, and $\eta = 135°$.

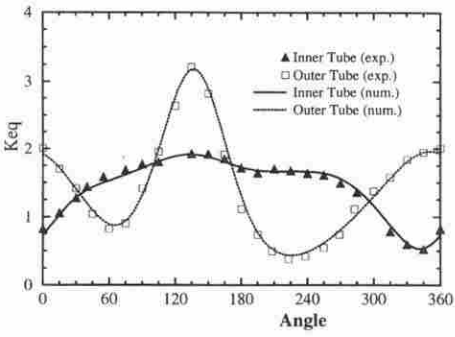

Figure 10. Comparison of the local equivalent conductivity for natural convection in an eccentric annulus at Ra = 10^3, Pr = 0.71.

Figure 10 shows comparisons between the experimental and numerical values of the local equivalent conductivities, where the angle is measured clockwise from the upward vertical axis. The local equivalent and average conductivities are in good agreement with the experimental results, as demonstrated in Figure 10 and Table 4.

CONCLUSION

This work outlines a modified full multigrid method. In this algorithm, only residuals are restricted from the fine grid by a way of summation, where the starting solutions on the coarse grid are taken from the previous cycle. There is no restriction procedure for the variables but only for the residuals. Nonmatching of mass fluxes does not pose a problem. This simplifies the multigrid strategy and the structure of the program. The treatment of the pressure correction equation on the coarse grid is achieved in a way similar to the other variables. The modified full multigrid version of the SIMPLE algorithm using collocated grids is shown to be efficient for the calculation of fluid flow and heat transfer, with a speed-up of up to 25.

REFERENCES

1. K. C. Karki, P. S. Sathyamurty, and S. V. Patankar, Performance of a Multigrid Method with an Improved Discretization Scheme for Three-Dimensional Fluid Flow Calculations, *Numer. Heat Transfer B*, vol. 29, pp. 275–288, 1996.
2. Z. Lilek, S. Muzafeija, and M. Perić, Efficiency and Accuracy Aspects of a Full-Multigrid SIMPLE Algorithm for Three-Dimensional Flows, *Numer. Heat Transfer B*, vol. 31, pp. 23–42, 1997.
3. D. S. Joshi and S. P. Vanka, Multigrid Calculation Procedure for Internal Flows in Complex Geometries, *Numer. Heat Transfer B*, vol. 20, pp. 61–80, 1991.
4. D. Rayner, Multigrid Flow Solutions in Complex Two-dimensional Geometries, *Int. J. Numer. Meth. Fluids*, vol. 13, pp. 507–518, 1991.
5. H. J. Leister and M. Perić, Numerical Simulation of a 3D Czochralski Melt Flow by a Finite Volume Multigrid Algorithm, *J. Crystal Growth*, vol. 123, pp. 567–574, 1992.
6. I. Demirdzic and M. Perić, Numerical Study of Grey-Body Surface Radiation Coupled with Fluid Flow for General Geometries Using a Finite Volume Multigrid Solver, *Int. J. Heat Fluid Flow*, vol. 6, pp. 3–18, 1996.

7. I. Demirdzic, Z. Lilek, and M. Perić, Fluid Flow and Heat Transfer Tests Problems for Non-orthogonal Grids: Bench-Mark Solutions, *Int. J. Numer. Meth. Fluids*, vol. 15, pp. 329–354, 1992.
8. P. Johansson and L. Davidson, Modified Collocated SIMPLEC Algorithm Applied to Buoyancy-Affected Turbulent Flow Using a Multigrid Solution Procedure, *Numer. Heat Transfer B*, vol. 28, pp. 39–57, 1995.
9. F. S. Lien and M. A. Leschziner, Multigrid Convergence Acceleration for Complex Flow Including Turbulence, *Int. Ser. Numer. Math.*, vol. 98, pp. 277–288, 1991.
10. F. S. Lien and M. A. Leschziner, Multigrid Acceleration for Recirculating Laminar and Turbulent Flows Computed with a Non-orthogonal Collocated Finite-Volume Scheme, *Comput. Meth. Appl. Mech. Eng.*, vol 118, pp. 351–371, 1994.
11. W. Shyy, M. H. Chen, and C. S. Sun, Pressure-Based Multigrid Algorithm for Flow at All Speeds, *AIAA J.*, vol. 30, no. 11, pp. 2660–2669, 1992.
12. P. G. Huang, B. E. Launder, and M. A. Leschziner, Discretization of Nonlinear Convection Processes: A Broad-Range Comparison of Four Schemes, *Comput. Meth. Appl. Mech. Eng.*, vol. 48, pp. 1–24, 1985.
13. S. V. Patankar, *Numerical Heat Transfer and Fluid Flow*, Hemisphere, Washington, DC, 1980.
14. J. H. Feriger and M. Perić, *Computational Methods for Fluid Dynamics*, Springer-Verlag, Berlin, Heidelberg, New York, 1996.
15. B. P. Leonard, A Stable and Accurate Convective Modelling Procedure Based on Quadratic Upstream Interpolation, *Comput. Meth. Appl. Mech. Eng.*, vol. 19, pp. 59–98, 1979.
16. B. van Leer, Toward the Ultimate Conservative Difference Scheme, B. V. A. Second-Order Sequel to Godunov's Method, *J. Comput. Phys.*, vol. 23, pp. 101–136, 1977.
17. C. M. Rhie and W. L. Chow, Numerical Study of the Turbulent Flow Past an Airfoil with Trailing Edge Separation, *AIAA J.*, vol. 21, pp. 1525–1532, 1983.
18. H. L. Stone, Iterative Solution of Implicit Approximations of Multidimensional Partial Differential Equations, *SIAM J. Numer. Anal.*, vol. 5, pp. 530–558, 1968.
19. J. Yan, L. Xue, T. Rung, and F. Thiele, A Modified Full Multigrid Algorithm for Navier-Stokes Equations, submitted to Int. J. Numer. Meth. Fluids.
20. U. Ghia, K. N. Ghia, and C. T. Shin, High-Re Solutions for Incompressible Flow Using the Navier-Stokes Equation and a Multigrid Method, *J. Comput. Phys.*, vol. 48, pp. 387–411, 1982.
21. G. de Vahl Davis, Natural Convection in a Square Cavity: A Bench Mark Numerical Solution, *Int. J. Numer. Meth. Fluids*, vol. 3, pp. 249–264, 1983.
22. Y. A. Koshmarov and A. Y. Ivanov, Experimental Study of Heat Transfer Through a Rarefied Gas between Coaxial Cylinders, *Heat Transfer, Sol. Res.*, vol. 5, no. 1, pp. 29–36, 1973.
23. S. D. Probert, D. Sadhu, and D. Syed, Thermal insulation provided by annular air-filled cavities, *Appl. Energy*, vol. 1, pp. 145–153, 1975.
24. E. van Sande and B. J. G. Hamer, Steady and transient natural convection in enclosures between horizontal circular cylinders, *Int. J. Heat Mass Transfer*, vol. 22, pp. 361–370, 1979.
25. D. Naylor, H. M. Badr, and J. D. Tarasuk, Experimental and Numerical Study of Natural Convection between Two Eccentric Tubes, *Int. J. Heat Mass Transfer*, vol. 32, pp. 171–181, 1989.
26. T. H. Kuehn and R. J. Goldstein, An Experimental Study of Natural Convection Heat Transfer in Concentric and Eccentric Horizontal Cylindrical Annuli, *ASME J. Heat Transfer*, vol. 100, pp. 635–640, 1978.